January, 2004
CERN/SPSC 2004-003
SPSC-M-711

ASACUSA STATUS REPORT

ASACUSA progress during 2003
and plans for 2004

ASACUSA collaboration

Contents

Summary

2003 Highlight - First observation of long-lived antiprotonic helium ions (2-body system)

All CPT-test experiments carried out until now by the ASACUSA collaboration dealt with the $\overline{p}\mathrm{He}^{+}$ atom which is a neutral three-body Coulomb system consisting of an antiproton, helium nucleus, and electron. The antiproton mass and charge have been determined to a precision of 10^{-8} by laser spectroscopy, but this relied heavily on the results of (difficult) 3-body QED calculations, which have errors similar to those of the measured laser transition frequencies.

In 2003, we have succeeded to produce long-lived ($\tau \sim 300 - 500$ ns) antiprotonic helium ions (two-body system: $\overline{p}\mathrm{He}^{++}$). This was done by stopping RFQD-decelerated antiprotons in a very low density helium gas target and selectively populating the ionic level by using a laser technique. In addition, we have found that their lifetimes depend on n, the principal quantum number of the orbiting $\overline{p}$.

The significance of this discovery is as follows:

1. Laser spectroscopy of $\overline{p}\mathrm{He}^{++}$ should be in principle possible, by inducing laser transitions between different n states, and make use of the n-dependent lifetimes to detect the resonance.

2. The ions are already thermalized and are cold ($T \sim 10K$). This is important to reach high precision in laser spectroscopy.

3. The antiproton mass and charge can be determined without being affected by the accuracy of the theoretical calculation.

Plans for 2004

In 2004, we plan to achieve the following:

1. Reach ppb-scale in antiprotonic helium atom (3-body) laser spectroscopy. A new laser system and a new frequency calibration system will make it possible to improve the present antiproton mass & charge precision of 10^{-8} by an order of magnitude.

2. First attempts at antiprotonic helium ion (2-body) laser spectroscopy. This requires a technically demanding high-power UV laser system, which is being prepared.

3. Optimization of the ultra low energy antiproton beam extraction efficiency out of the ASACUSA trap, continuation of this year's efforts.

4. Measurement of ionization cross section of helium (and hydrogen) by low energy antiproton impact.

Part I
ASACUSA Progress during 2003

1 First observation and systematic study of long-lived antiprotonic helium ions

1.1 Introduction

Until recently, all spectroscopy experiments carried out by the ASACUSA collaboration dealt with the $\overline{p}\mathrm{He}^+$ atom [1–3] which is a neutral three-body Coulomb system consisting of an antiproton, helium nucleus, and electron. During the years 2000–2002, several atomic transition frequencies were measured to a precision of six parts in 10^8 by laser spectroscopy [4, 5]. By comparing these with the results of theoretical calculations [6–8] and the antiproton cyclotron frequency measured by the TRAP collaboration [9], a new limit of one part in 10^8 was obtained for any possible differences $\delta_{\overline{p}}$ between the antiproton charge and mass, and those of the proton's. This derivation critically relied on accurate theoretical values [6–8] of the $\overline{p}\mathrm{He}^+$ energy levels, including higher-order relativistic and QED corrections of the electron. Even the most advanced calculations, however, currently have errors similar to those of the experimental transition frequencies (i.e. $\sim 10^{-8}$). Further improvements on $\delta_{\overline{p}}$ cannot be made without improving the theoretical precision, and these efforts are currently being made by two groups using the CERN LXPLUS and RIKEN VPP computer systems. At the same time, we also began examining the possibilities of extending our high-precision experiments to a two-body antiprotonic ion, that does not contain the perturbing electron responsible for all the theoretical difficulties described above.

In 2003, we produced and systematically studied for the first time large numbers ($N \sim 10^9$) of cold (temperature $T \sim 10$ K), long-lived antiprotonic helium $\overline{p}\mathrm{He}^{2+}$ ions. These are singly-charged two-body systems composed of only a helium nucleus and an antiproton which occupies a circular state with principal and angular momentum quantum numbers $n \sim 30$ and $\ell = n - 1$. Its energy level diagram (Fig. 1) has a much simpler structure compared to the three-body $\overline{p}\mathrm{He}^+$ case, the levels having the same n-values being degenerate. The states are unique in atomic physics as they constitute a truly ideal, classical Bohr system whose spin-independent parts of the energy levels can be theoretically calculated to a very high precision ($\sim 10^{-9}$) using the simple equation,

$$E_n = -4\frac{M}{m_e}\frac{R_\infty hc}{n^2}\frac{{Q_{\overline{p}}}^2}{e^2}, \tag{1}$$

where the antiproton reduced mass and electron mass are denoted by M and m_e, R_∞ is the Rydberg constant, and $Q_{\overline{p}}$ is the antiproton charge. By comparison for the 2p-state of atomic hydrogen, relativisitic corrections to the above equation appear at a level of $\sim 10^{-5}$ and QED corrections at $\sim 10^{-6}$. These effects are very small in the $\overline{p}\mathrm{He}^{2+}$ case because of the large antiproton mass, its small magnetic moment, and the circular orbital which has very little overlap with the helium nucleus. The simple idealised Bohr system

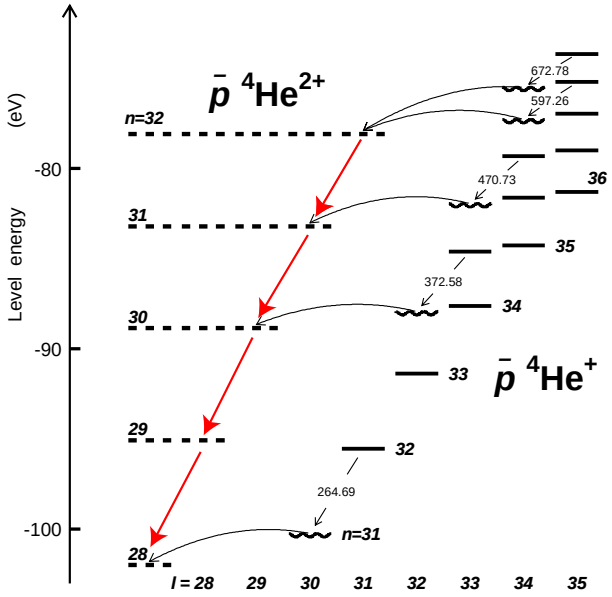

Figure 1: Energy level diagram of $\overline{p}^4\mathrm{He}^{2+}$ ions and $\overline{p}^4\mathrm{He}^{+}$ atoms. Wavelengths of five $\overline{p}^4\mathrm{He}^{+}$ transitions used to ionize the electron are indicated in nanometers. Curved lines indicate Auger transitions to ionic states, red arrows radiative transitions in the $\overline{p}\mathrm{He}^{2+}$ ion.

can easily be shown to have typical lifetimes near $n = 30$ of $\tau \sim 300$–500 ns against annihilation, as the antiproton undergoes a series of slow radiative transitions of the type $\Delta n = \Delta \ell = -1$ (indicated using red arrows). Due to the theoretically-expected longevity and ease in calculating the energy levels, the ion is expected to be an ideal candidiate for future measurements on the properties of antiprotons.

1.2 Creation and fate of $\overline{p}\mathrm{He}^{2+}$ ions

Antiprotonic helium ions can be created in $\overline{p}$-helium atom collisions either by direct scattering, or by first forming the familiar neutral atom (the object studied previously by our collaboration), which subsequently ejects its electron in an Auger transition. These processes occur at a typical antiproton kinetic energy of ~ 10 eV. In the direct formation case, the ions, statistically distributed over a wide range of n- and ℓ-values, recoil vigorously with initial temperature $T \sim 10^4$ K. The probable reason why ions have never been observed in our past experiments is they are expected to be rapidly destroyed by collisions with ordinary helium atoms in the target. Indeed, cascade calculations [10–13] predict that for liquid helium densities (atomic density $\rho \sim 10^{22}$ cm^{-3}) the antiproton annihilates with femtosecond-scale lifetimes, primarily due to collisional Stark mixing effects. The same is probably true for all helium densities that we have used in our previous experiments; under these conditions only certain 'metastable' states of the three-body $\overline{p}\mathrm{He}^{+}$ (possessing an extra electron which shields the antiproton during collisions with other helium atoms) can be expected to survive long enough to allow laser spectroscopy to be

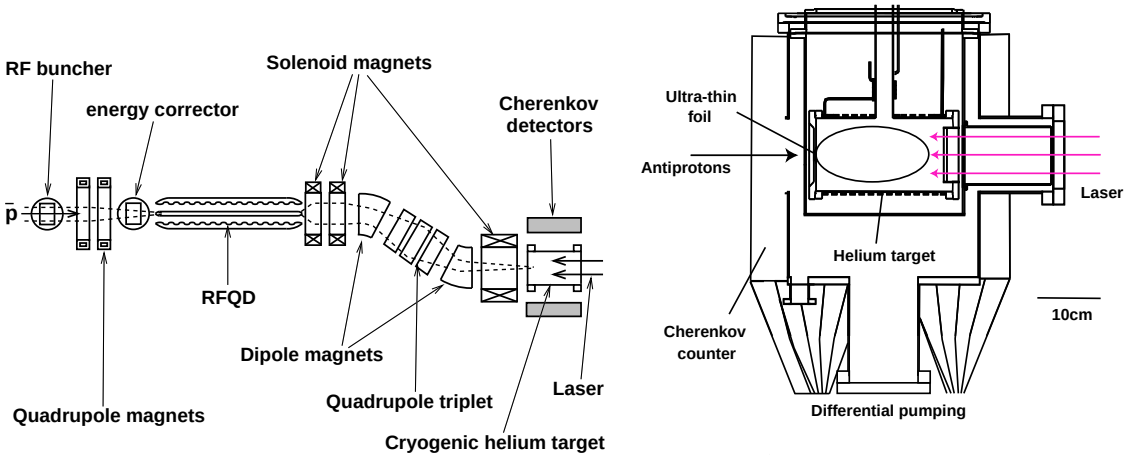

Figure 2: Experimental layout.

carried out.

1.3 Technique for observing $\overline{p}\mathrm{He}^{2+}$ ions

The above reasoning suggested that if the $\overline{p}\mathrm{He}^{2+}$ ions could be brought to rest in extremely low density helium, collision-induced annihilation would be drastically reduced, permitting it to survive for a much longer time. This should become evident as a prolongation of the decay time of the tail of the spike produced in the annihilation rate when metastable to Auger-dominated transitions are induced in $\overline{p}\mathrm{He}^{+}$ by resonant laser irradiation.

We therefore attempted to produce 100-ns-scale lifetime ions of both the $\overline{p}^4\mathrm{He}^{2+}$ and $\overline{p}^3\mathrm{He}^{2+}$ isotopes by stopping antiprotons in a helium target with the lowest practically achievable density ($\rho \sim 10^{15}$ cm^{-3}). This was 100 times lower than the typical densities used in 2002 for the high-precision laser spectroscopy experiments utilizing the RFQD described above, and 10^5–10^6 times more dilute than the first expeeriments carried out at the AD in 2000–2001). The metstable three-body $\overline{p}\mathrm{He}^{+}$ so created were able to survive many collisions with the surrounding helium atoms, and cooled within 100 ns to a temperature $T \sim 10$ K, this being inferred from the Doppler widths of the $\overline{p}\mathrm{He}^{+}$ laser resonances. Resonant laser irradiation and the proceeding Auger process then removed the remaining electron to form a $\overline{p}\mathrm{He}^{2+}$ ion with roughly the same temperature $T \sim 10$ K as the neutral atom. For example, a laser pulse of wavelength $\lambda = 597.3$ nm (Fig. 1) was used to induce an atomic transition from the long-lived $\overline{p}^4\mathrm{He}^{+}$ state $(n, \ell) = (39, 35)$ to the state $(n, \ell) = (38, 34)$ having a theoretical Auger lifetime of several nanoseconds. This lead to electron emission and the formation of a $\overline{p}\mathrm{He}^{2+}$ occupying the ionic state $(N, L) = (32, 31)$.

1.4 Experimental realization

The experimental setup was similar to the one used last year [5], but numerous modifications (particularly in the helium target, laser system, and detectors) were made to achieve the much lower target densities, and higher time resolutions and laser energies, all of which were needed for unambiguously demonstrating the production of $\overline{p}\mathrm{He}^{2+}$ ions.

The AD produced a 100-ns-long pulsed beam containing 3×10^7 antiprotons of energy $E = 5.3$ MeV. A radiofrequency quadruopole decelerator (RFQD) was used to decelerate some $\sim$ 30% of the antiprotons to an energy $T = 65$ keV, while the remaining 70% emerged with little or no deceleration. The decelerated antiprotons were diverted by an achromatic momentum analyzer connected to the output of the RFQD, and focused into the entrance of a helium gas target; this diversion eliminated the large background that the undecelerated antiprotons would have otherwise produced. The spatial profiles of antiproton pulses along the beam line were measured non-destructively by four micro-wire secondary electron emission detectors. The target was a 150-mm-diameter, 300-mm-long cylindrical chamber filled with ^{4}He or ^{3}He gas at temperature $T \sim 10$ K. By carefully adjusting the RFQD output energy, tuning the AD electron cooling to minimize the energy spread of the antiproton beam, and using an ultra-thin target entrance window of higher uniformity, we managed to stop antiprotons within the volume of the target chamber at target densities down to $\rho \sim 3 \times 10^{15}$ cm^{-3} (corresponding to a pressure $P = 4 \times 10^{-2}$ mbar, i.e. 100 times lower than the typical values used in 2002).

The $\overline{p}\mathrm{He}^{+}$ were irradiated by high-power (P = 20–60 mJ/4 ns) laser pulses with wavelengths $\lambda = 264$–726 nm and durations $\Delta t = 4$–6 ns, which were produced by a four-stage dye laser amplifier developed this year. The laser beam was expanded to a diameter $d = 12$ cm using a telescope containing a 15-cm-diam, UV-transparent lens, entered the target through a fused silica window, and retro-reflected from the polished surface of a vacuum flange mounted on the other side. As in all our laser-spectroscopy experiments, charged pions produced by the annihilation of the ion were detected by plastic Cherenkov counters surrounding the target; new versions of these in the present experiment were equipped with gatable micro channel plate photomultipliers, which measured the envelope of the Cherenkov light with sub-nanosecond time resolution. By recording the resulting waveform with a digital oscilloscope, delayed annihilation time spectra (the distribution of the number of antiproton annihilations, as a function of time elapsed since atomic formation) were observed.

1.5 Unambiguous observation of several ionic states

In Fig. 3 (a), the laser-induced spike appearing in the delayed annihilation time spectrum measured at the high target density of $\rho = 5 \times 10^{21}$ cm^{-3} is shown. The spike decayed with a lifetime $\tau \sim 6$ ns, which indicates that the ion is rapidly destroyed by collisions at this density. When the same transition was measured (b) under the conditions of the present experiments, i.e. $\rho = 3 \times 10^{16}$ cm^{-3}, the lifetime increased by an order of magnitude to $\tau_{\mathrm{s}} \sim 30$ ns [Fig. 3 (b)] as was expected from the prolonged collisional lifetime of the $\overline{p}\mathrm{He}^{2+}$ ion [initially occupying ionic state $(N, L) = (31, 30)$ in this example].

By inducing various laser transitions, we systematically measured the time until anni-

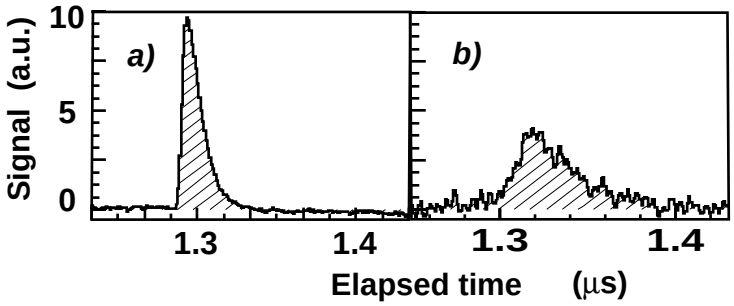

Figure 3: Laser spike of $\overline{p}^4\mathrm{He}^+$ transition $(37,34)\rightarrow(36,33)$ measured at high (a) and ultra-low (b) densities.

hilation for ions occupying four $\overline{p}^4\mathrm{He}^{2+}$ [i.e. those with $(N,L)=(32,31)$, $(31,30)$, $(30,29)$, and $(28,27)$] and $\overline{p}^3\mathrm{He}^{2+}$ [$(31,30)$, $(30,29)$, $(29,28)$, and $(28,27)$] states. In Fig. 4, the decay rates of the spikes are plotted as a function of target density between $\rho = 3\times10^{15}$ and 2×10^{18} cm^{-3}. In the region $\rho < 10^{18}$ cm^{-3}, the annihilation rates increased as a linear function of density. At higher densities it saturated due to i): the finite time resolution of the 4–6-ns-long laser pulse, and ii): the Auger lifetime of the parent $\overline{p}\mathrm{He}^+$ state [14], which varied from 10 picoseconds to a few nanoseconds. Extrapolation to $\rho = 0$ yielded lifetimes $\tau = 100$–500 ns consistent with the theoretical values of a single isolated $\overline{p}\mathrm{He}^{2+}$ ion within error bars.

We fitted a linear function on the low-density part of the data shown in Fig. 4, and plotted its gradient in Fig. 5 as a function of the ionic principal quantum number N. We found that states with large N-values have shorter collisional lifetimes; this qualitatively agrees with the naive assumption that higher states with large atomic radii have correspondingly larger collisional cross-sections. The lifetimes of $\overline{p}^3\mathrm{He}^{2+}$ had a stronger dependence on N compared to those of $\overline{p}^4\mathrm{He}^{2+}$; the reason for this is not understood. These experimental results are crucial in developing methods to carry out laser or microwave spectroscopy of these ions in the future.

2 Auger rate measurements and the complex energy of $\overline{\mathrm{p}}\mathrm{He}^+$

As mentioned in the previous section, new CPT-violation limits on the antiproton mass and charge were determined [5] by measuring some transition energies of the $\overline{p}\mathrm{He}^+$ atom to a precision of 50–200 ppb. In addition to the level energies E_r, an important property of the states of the $\overline{\mathrm{p}}\mathrm{He}^+$atom is their decay rate γ, which forms the imaginary part of the complex energy,

$$E = E_r - i\frac{\gamma/2\pi}{2}. \tag{2}$$

In particular, the Auger rates γ_A, which are dominant in the total decay rate for some $\overline{p}\mathrm{He}^+$ states, have been calculated by many theorists [32–35] over a period of more than

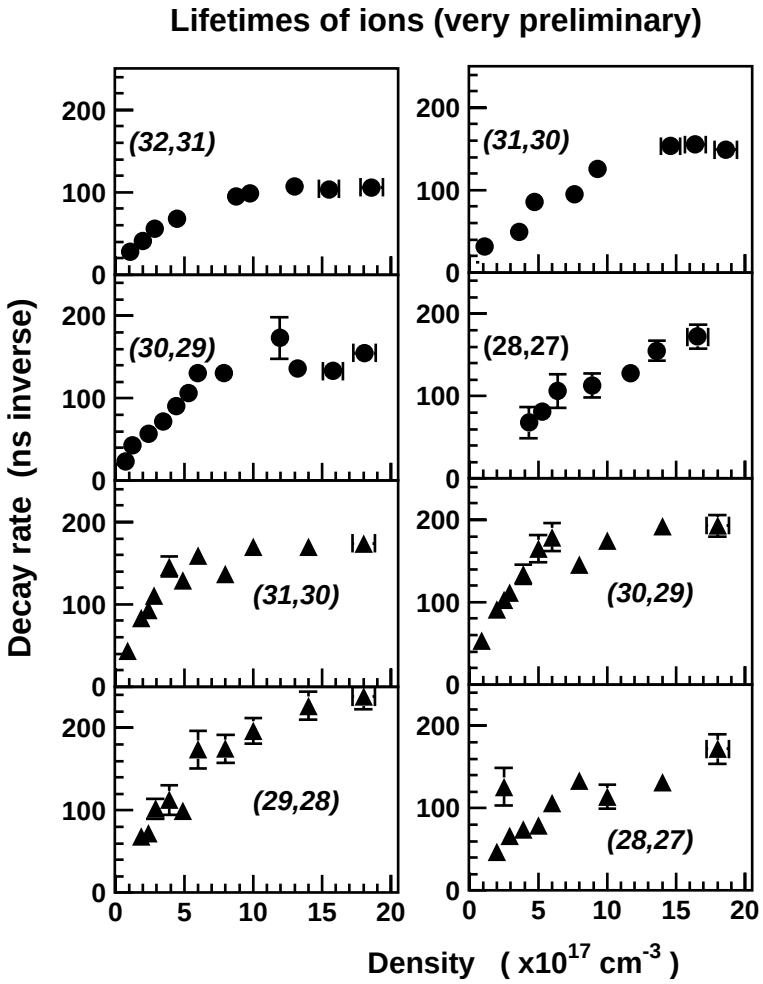

Figure 4: Decay rates of annihilation signals measured at various target densities: data corresponding to $\overline{p}^4\mathrm{He}^{2+}$ states plotted using filled circles, those of $\overline{p}^3\mathrm{He}^{2+}$ plotted using triangles.

30 years. The latest calculations with CCR (Complex Coordinate Rotation) method by Korobov [8] and Kino [36] yield both real and imaginary parts of the complex energy at the same time, and the both parts are expected to have absolute precisions of the same order. An independent check on the validity of these three-body calculations can therefore be obtained by measuring the decay rates of Auger-dominant states.

In 2003, the decay rate of the (34, 31) state of $\overline{p}^3\mathrm{He}^+$was determined by measuring the natural width of the laser resonance of the (33, 32) $\rightarrow$ (34, 31) transition (shown in Fig. 6), The measurement of this decay rate is of great importance as there is a large discrepancy between the two CCR calculations. The result was anomalously large compared to a typical value approximated from the lowest possible transition multipolarity or one theoretical value [8], but was not, however, far away from the other theoretical values. The reason for the anomaly was supposed to be due to a state mixing with an electron-excited configuration having a nearby level energy. Namely, the configuration $(30, 29)_{\bar{p}} \otimes (3d)_e$

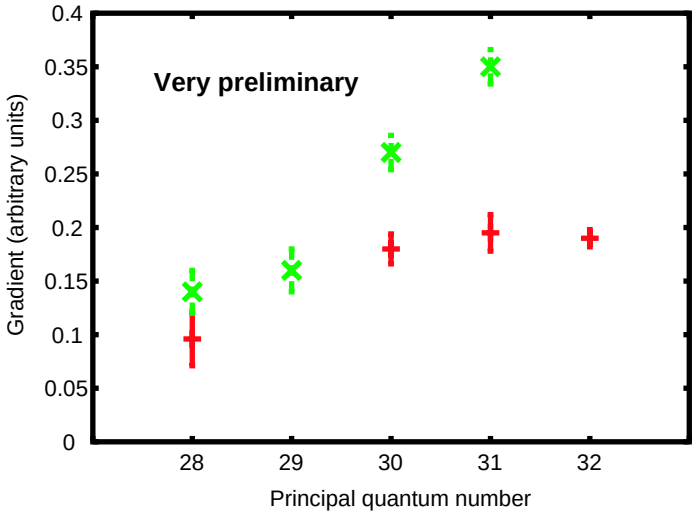

Figure 5: Gradient of annihilation rate/target density of four $\overline{p}^4\mathrm{He}^{2+}$ (indicated in red) and $\overline{p}^3\mathrm{He}^{2+}$ (green) ionic states, plotted as a function of the principal quantum number n. This data is essential in developing methods to carry out laser or microwave spectroscopy of the ion.

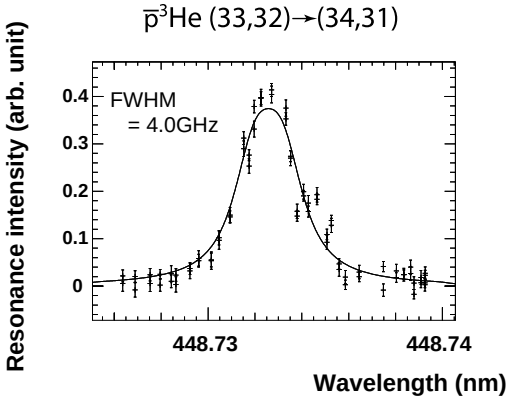

Figure 6: Laser resonance profile of the (33, 32) → (34, 31) transition of $\overline{p}^3\mathrm{He}^+$.

Experimental value	KRB-SMM [34]	KRB [8]	KNO [36]
$(1.84 \pm 0.65) \times 10^{10}$	3.5×10^{10}	6.7×10^{7}	1.09×10^{11}

Table 1: Experimental and four theoretical decay rates of the (34, 31) state of of $\overline{p}^3\mathrm{He}^+$in s^{-1}. The typical decay rate, approximated from the lowest possible transition multipolarity of the Auger transition from this state ($L = 3$), is 10^8 s^{-1}.

was coupled to the (34, 31) state of $\overline{p}^3\mathrm{He}^+$, which has a nearby energy, and caused the decay rate enhancement. The possibility of such influence by an electron-excited state

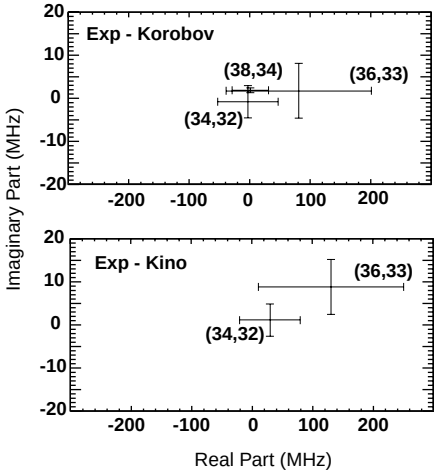

Figure 7: Precise comparison of the complex energies of three $\overline{p}^4\mathrm{He}^+$ states. The difference of the experimental values from the two theories [8,36] are plotted in MHz. The imaginary part plotted here is the half Auger width with negative sign, $-\frac{1}{2}(\gamma_A/2\pi)$. The values used for the comparison of the real part are the transition frequencies from metastable states, where the theoretical uncertainty should be very small.

was already pointed out by Kartavtsev [35].

By using the results of 2001–2003, we were able to expand the recent precise experiment-theory comparison of the level energies [5] to the complex plane. In Fig. 7, the complex energy, defined as Eq. (2), was compared with values from two theories, [8] and [36]. For the imaginary part (*i.e.* the half Auger width) of the three $\overline{p}^4\mathrm{He}^+$ states presented in Fig. 7, no discrepancy greater than 10 MHz, was found. This limit is absolutely even more precise than that obtained for the real part (i.e. the level energy).

3 Study of the hyperfine structure of antiprotonic helium

In 2003 we performed systematic studies of the hyperfine structure (HFS) of the $(n, L) = (37, 35)$ state of antiprotonic helium, which was first measured in 2001. The hyperfine structure of $\overline{p}\mathrm{He}^+$ is a consequence of the interaction of the magnetic moments of the electron and the antiproton, and is unique due to the large angular momentum $\vec{L}_{\overline{p}}$ of the antiproton. It leads to a splitting of each state (n, L) into a quadruplet (cf. Fig 8), with the dominant splitting arising from the interaction of $\vec{L}_{\overline{p}}$ with the electron spin $\vec{S}_e$ with angular momentum $\vec{F} = \vec{L}_{\overline{p}} + \vec{S}_e$ (called *hyperfine* (HF) splitting). The interaction of the antiproton spin $\vec{S}_{\overline{p}}$ with the other moments leads to a further splitting called *superhyperfine* (SHF) splitting, where the total angular momentum is given by $\vec{J} = \vec{F} + \vec{S}_{\overline{p}}$.

The experiment uses a laser-microwave-laser resonance method: since all SHF levels are thermally equally populated, a laser pulse at $t = t_1$ of frequency f_+ is used to transfer

a large fraction of the population of the F^+ doublet to a short-lived daughter state, from where the $\overline{p}$ quickly annihilates with a nucleon of the He nucleus. Microwave radiation resonant with $\nu_{\rm HF}^-$ or $\nu_{\rm HF}^+$ transfers population from the F^- doublet to the F^+ one, and a second laser pulse of frequency f_+ measures the population of the F^+ doublet at time $t_2 > t_1$. We fire two subsequent laser pulses of constant frequency into the helium target, while scanning the frequency $\nu_{\rm MW}$ of microwave radiation applied between t_1 and t_2. Each laser pulse leads to a spike in the analogue delayed annihilation time spectrum (ADATS), whose area $I(t)$ is proportional to the population of the level F^+ at time t. We therefore measure the ratio $R = I(t_2)/I(t_1)$ as a function of $\nu_{\rm MW}$, expecting an increase if $\nu_{\rm MW}$= $\nu_{\rm HF}^{\pm}$.

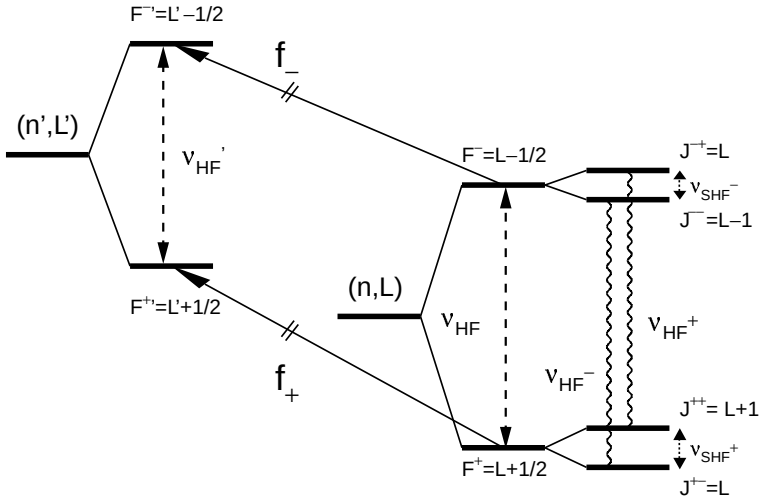

Figure 8: Schematic view of the HF and SHF splitting of a $\overline{p}$He$^+$ state (n, L), and laser transitions to a short-lived daughter state (n', L'). Only laser transitions between HF states are shown because our laser system cannot resolve transitions between SHF levels. Wavy lines denote allowed magnetic transitions associated with an electron spin flip.

In 2001 we measured for the first time the two microwave induced transitions with frequencies $\nu_{\rm HF}^+$ and $\nu_{\rm HF}^-$, resp., with a relative precision of 3×10^{-5} [15]. The values agree with recent theoretical calculations [16–18] on a level of 6×10^{-5}, which roughly corresponds to the estimated theoretical accuracy. The experiment has fully confirmed the presence of a quadruplet structure originating from the hyperfine coupling, as predicted by Bakalov and Korobov [16] (cf. Fig. 8 (left)). The measured microwave resonance frequencies, $\nu_{\rm HF}^+$ and $\nu_{\rm HF}^-$, are primarily sensitive to the $\overline{p}$ *orbital* magnetic moment, and constitute a first measurement of the orbital g-factor for either proton or antiproton with an accuracy of 6×10^{-5}. On the other hand, the splitting between $\nu_{\rm HF}^+$ and $\nu_{\rm HF}^-$ is caused by the $\overline{p}$ spin magnetic moment $\vec{\mu}_{\overline{p}}$ which is currently known with a precision of 0.3% [19]. The experimental error on $\nu_{\rm HF}^+ - \nu_{\rm HF}^-$ is much larger that the precision on each frequency, yielding a value for $\vec{\mu}_{\overline{p}}$ with an error of 1.6%. The theoretical precision for $\nu_{\rm HF}^- - \nu_{\rm HF}^+$ is the same as for each value separately (5×10^{-5}), so that no new calculations are needed if the experimental precision could be improved.

A better experimental accuracy can only be achieved if the line width Γ can be reduced. The beamtime in 2003 was therefore focussed on a systematic study of Γ. The width of the resonance lines in the first experiments was $\gamma_{\rm exp} = 5.3 \pm 0.7$ MHz, which can have the following reasons:

1. Fourier limit of the observation time window.
   We generate the two subsequent laser pulses by splitting one pulse and delaying part of it by multiple reflections between mirrors. A maximum delay of $\Delta t = t_2 - t_1 = 140$ ns could be achieved this way without disturbing the spatial profile of the laser beam too much. Thus the applied microwave pulse is a sine wave multiplied by a rectangular pulse of 140 ns length. The Fourier transform of such a signal leads to a $\sin^2(\nu)/\nu^2$ structure which has a FWHM given by $\Delta\nu = 2.78/(\pi\Delta t) = 6.3$ MHz, which is in agreement with the observed value.

2. Collisional broadening.
   The E1 laser transitions between states (n, L) and (n', L') are known to have both a strong density shift and a large collisional broadening [20]. For the M1 transitions induced by microwave, this is intuitiveley expected to be much smaller. Theoretical calculations by Korenman [21, 22] and Bakalov [23] agree that the shift of the line centres with density is very small, but disagree on the magnitude of collisional broadening at our densities. While Bakalov predicts it to be or as small as 10 kHz [23], Korenman estimates that the broadening can be of the order of MHz [22] at our previous experimental conditions (6.1 K and 250 or 530 mbar), close to the experimental value.

3. Residual constant magnetic field.
   A residual static magnetic field leads to Zeeman splitting of the HF and SHF states. Since the direction of $\vec{S}_e$ in the F^+ and F^- states is opposite, levels with the same magnetic quantum numbers m of these states undergo Zeeman shifts of opposite sign. Thus, the broadening of the transition energy by a constant magnetic field B_0 is doubled. Since the microwave resonance is allowed for $(F^+, m) \rightarrow (F^-, m')$ with $m' = m - 1, m, m + 1$, the resonance frequency is split into many lines lying in the range of $\nu = \nu_{HF} \pm \Delta\nu$ with

   $$\Delta\nu \sim 2\ B_0\ \mu_B/\hbar \sim 2.8\ \text{MHz/Gauss}. \tag{3}$$

   To reduce this effect, we employed a mumetal shield. This reduced the residual magnetic field measured at the stopping position of the antiprotons to $B_0 \leq 0.01$ Gauss. Unless some of the welds of our stainless steel cavity become magnetic at low temperatures, the resulting broadening is much smaller than the observed line width.

4. Further sources of broadening, namely power broadening, the effect of the inhomogeneity of the oscillating magnetic field (we us a TM110 cavity mode), and the dependence of the Rabi frequency on the magnetic quantum number m, have been evaluated by a numerical simulation. The results show [24] that none of these lead to a significant broadening.

Our goal was to investigate points 1 and 2 by changing the time window Δt and the target density. But it turned out that the experiment was very difficult due to the requirements on the antiproton beam. The first experiment as well as numerical simulations [24] show that at best a 10 % increase of $I(t)$ can be expected on resonance, because the broad-band pulsed laser we use allows us only to achieve a depopulation efficiency of ~ 30 %. This is much less than the typical shot-to-shot fluctuations of $I(t)$. Furthermore the sensitivity is very much reduced if a large fraction of the $\overline{p}$ are not stopped in the helium gas but in the surrounding material. Antiprotons stopped there produce a background by $\pi^+ \rightarrow \mu^+ \rightarrow e^+$ decay with the muon lifetime, which reduces $I(t)$. Unlike in our first run in 2001, this year the 5 MeV AD beam at our target position showed a significant beam halo which was much wider than our entrance window. We spent the largest fraction of out 4 week beam time trying to observe a signal, and succeeded only when either reducing the AD beam intensity by ~ 40 % or turning off the bunch rotation which compresses the AD pulse from 200 to 100 ns length, thus reducing the space charge in the AD pulse.

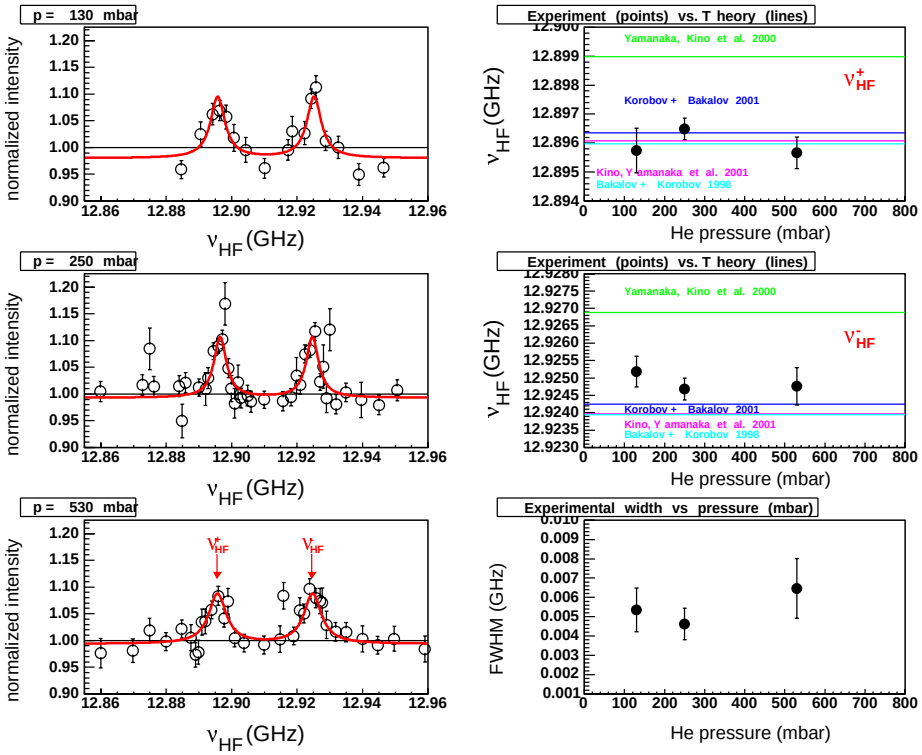

Figure 9: Left: Microwave resonance scans for the newly measured helium gas pressure of 130 mbar (top scan) and two previously measured pressures (250 and 530 mbar). Right: Dependence of ν^-_{HF}, ν^+_{HF} and the Lorentzian width of the resonance lines on the target pressure.

Studies of our laser system showed that it is impossible to enlarge the time window Δt between the two laser pulses beyond the achieved 140 ns without seriously degrading the lateral laser profile. This leads to a highly reduced depopulation efficiency, making the experiment impossible. To achieve a lower target density, we first tried to use higher

temperature of the target gas. It turned out, however, that at higher temperature the collisional broadening of the *laser* lines is much larger, leading to an overlap of the f_- and f_+ lines which reduces the population asymmetry. Therefore the only solution was to reduce the density below the previously lowest value (6.1 K and 250 mbar). Since this leads to an enlargement of the antiproton stopping distribution, a larger fraction of $\overline{p}$ stops outside the laser beams and also reduces $I(t)$. The density could be lowered at maximum by a factor 2 to 130 mbar at 6.1 K. Fig. 9 (left) shows the resulting microwave scan, together with data taken in 2001 at 250 and 530 mbar. In Fig. 9 (right) the two transition frequencies and the width of the resonance line is plotted against the density. The new result clearly confirms that *i)* there is no density shift within the experimental errors visible and *ii)* the value $\nu^+_{\rm HF}$ agrees very well with the theoretical results, while $\nu^-_{\rm HF}$ seems to be systematically larger than predicted. The observed width at 130 mbar is very similar to the other and more or less independent of the density. This indicates that the Fourier limit due to the time interval of $\Delta t = 140$ ns is the limiting factor for the experimental resolution.

An improvement of the experimental resolution is only possible if Δt can be enlarged, and the stability and quality of the antiproton beam is improved. The first factor requires a completely new laser system with two independent pulse-amplified cw lasers which is being developed by us. The second requirement might only be fulfilled if a slow extracted $\overline{p}$ beam would become available. In this case the $\pi^+ \rightarrow \mu^+ \rightarrow e^+$ background can be eliminated by requiring a pion multiplicity of at least two for each annihilation event.

4 Temperature dependence of the quenching cross section of $\overline{p}\mathrm{He}^+$ atoms in collisions with hydrogenic molecules

During the measurements in 2002, quantum tunnelling effects were revealed in collisions of $\overline{p}\mathrm{He}^+$ atoms with H_2 and D_2 molecules [25, 26]. According to the theoretical calculations [27], an (n, l)-dependent activation barrier exists for this kind of collisional reaction, where n and l are the principal and orbital quantum numbers of the $\overline{p}\mathrm{He}^+$ atom. For this theoretical model, the temperature (T) dependence of the collisional quenching cross section σ_q of the $\overline{p}\mathrm{He}^+$ atom can be expressed as a sum of an Arrhenius-type term and a temperature-independent term:

$$\sigma_q = \sigma_0 \exp(-E_b/kT) + \sigma_t, \tag{4}$$

where σ_0 is the cross section at infinitely high temperatures, E_b is the height of the activation barrier, k is the Boltzmann constant, and σ_t is the cross section of tunnelling of the colliding H_2 or D_2 molecule through the activation barrier. By measuring σ_q at different temperatures, E_b and σ_t can be obtained. In 2002, we could only measure the detailed temperature dependence of the state $(38, 37)$ with D_2 (see Fig. 10) [25, 26], therefore in 2003, we extended the measurements to other states and lower temperatures (down to 15 K instead of the previous 25 K).

The experimental method was the same as in previous years [25]. To obtain the

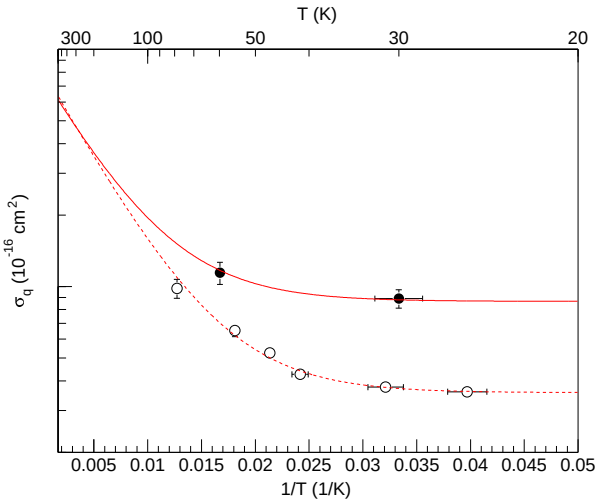

Figure 10: Quenching cross section σ_q of the state $(38, 37)$ versus the inverse temperature $1/T$, as measured in 2002. At low temperatures, where the term $\sigma_0 \exp(-E_b/kT)$ in Eq. (4) is negligible, σ_q levels off to σ_t. From [25].

quenching cross section σ_q, the decay rate γ of the state was measured at different admixture molecule (H_2 or D_2) number densities $n_{\rm adm}$. Assuming binary collisions, γ can be expressed as [25]

$$\gamma = \gamma_0 + n_{\rm adm}\, v_{\rm th}\, \sigma_q, \tag{5}$$

where γ_0 is the 'intrinsic' decay rate of the state in pure helium, and $v_{\rm th} = \sqrt{8kT/(\pi M_{\rm red})}$ is the relative velocity of the colliding molecules (where k denotes the Boltzmann constant, T the target gas temperature, and $M_{\rm red}$ the reduced mass of the colliding system). The left subfigure of Fig. 11 shows a plot of the decay rate γ versus the flux $n_{\rm adm} v_{\rm th}$; the quenching cross section σ_q can be determined by fitting the above equation to the data points (see the straight line in the subfigure). The decay rate of a metastable state was measured using the t1-scan method [28].

During the 5 shifts which were allocated for these measurements, we measured the state $(39, 35)$ with D_2, and the state $(37, 34)$ with H_2 in detail. Besides, we measured one σ_q point for the state $(39, 35)$ with H_2, and a few decay rates in pure helium to verify that the decay rate is independent of the target pressure. The obtained quenching cross sections are listed in Table 2, and plotted – together with the previously measured ones [29, 30] – in Fig. 12.

The cross section of the state $(39, 35)$ with D_2 at 60 K has a very large error (see the left-most point in the left subfigure of Fig. 12). This large error can be understood by looking at the right subfigure of Fig. 11 which shows that the decay rates measured with D_2 concentrations of 10 ppm (at 5 bar) and 30 ppm (at 1 and 2 bar) are inconsistent. The too large decay rate at 10 ppm and 5 bar might be caused by oxygen contamination, since oxygen molecules are known to quench $\bar{p}He^+$ atoms violently. At 60 K, the maximum (saturation) vapour pressure of O_2 is ∼10.4 mbar, which can cause a maximum decay rate of ∼150 μs^{-1}, assuming a quenching cross section of $\sigma_q(O_2) = 20{\times}10^{-16}$ cm^2 [31].

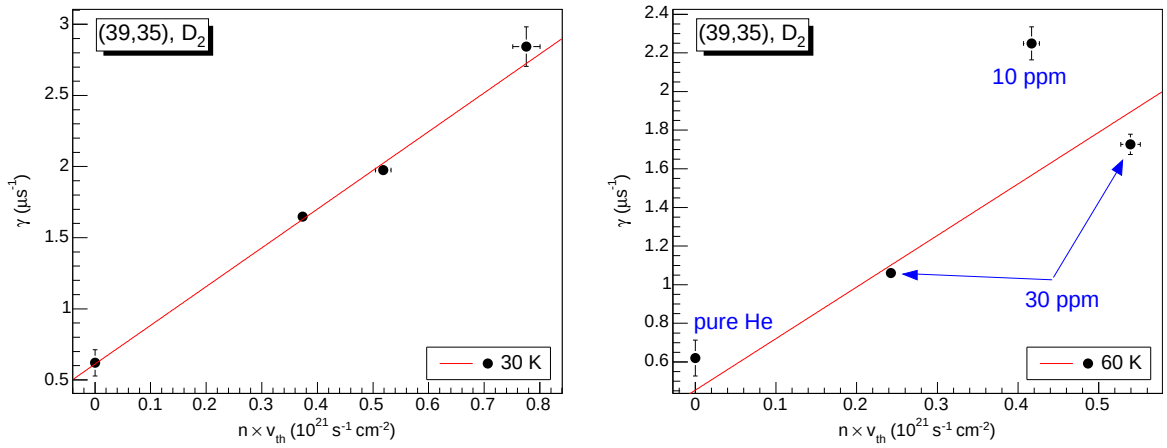

Figure 11: Decay rate of the state $(39, 35)$ versus the flux $n \times v_{\text{th}}$ of the D_2 molecules. Left: measured at 30 K. Right: measured at 60 K. All values are preliminary.

Table 2: Quenching cross sections σ_q, measured in 2003. All values are preliminary.

(n, l)	adm.	T (K)	σ_q (10^{-16} cm^2)
$(39, 35)$	H_2	15.0(10)	39.3(29)
	D_2	15.1(11)	36.0(43)
		17.0(10)	32.5(54)
		20.0(10)	30.9(31)
		29.8(11)	27.2(19)
		40.4(10)	24.8(17)
		60.6(13)	26.7(111)
$(37, 34)$	H_2	15.1(10)	1.31(27)
		20.1(10)	1.04(20)
		60.5(12)	1.47(12)

If we assume that the 10-ppm–5-bar point is incorrect and only fit the other two points (plus the pure helium point), we obtain $(21.4 \pm 1.8) \times 10^{-16}$ cm^2 for the quenching cross section. (This value is drawn with an empty square in the right subfigure of Fig. 12.)

The observed temperature dependence of the quenching cross sections caused some surprises. The data show that the quenching cross section of the state $(39, 35)$ increases with decreasing temperature. According to the theoretical calculations [27], this state does not have an activation barrier (i.e. the potential between the $\overline{p}\text{He}^+$ atom and the H_2/D_2 molecule is always attractive), therefore one might expect a temperature-independent cross section close to the geometrical cross section, which is in strong contradiction to the measured data. Besides, the measured cross section at the lowest temperature is almost twice as large as the geometrical cross section. The most probable cause for such a behaviour is the increased attraction between the $\overline{p}\text{He}^+$ atom and the H_2/D_2

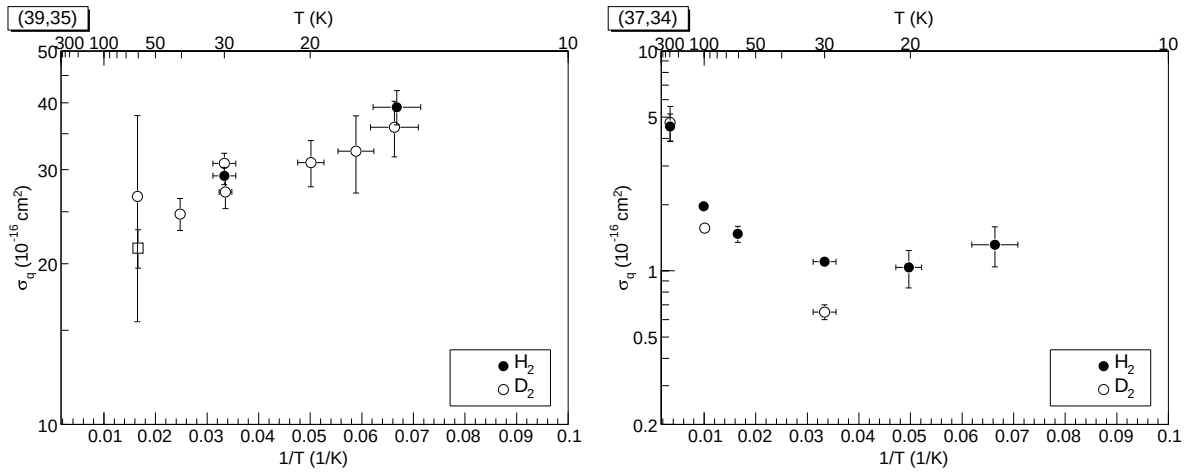

Figure 12: Logarithm of the newly (see Table 2) and previously measured quenching cross sections σ_q of the states $(39, 35)$ and $(37, 34)$ versus the inverse temperature $1/T$.

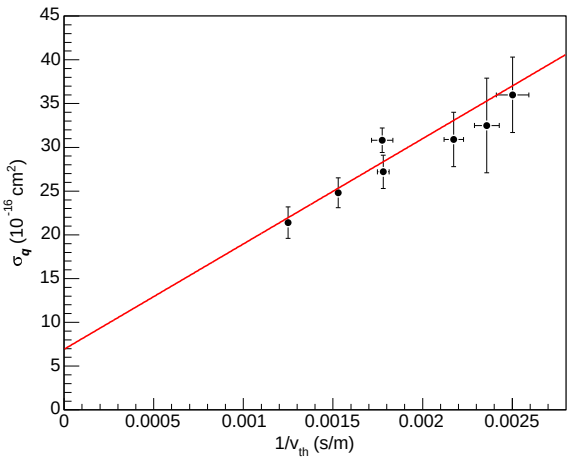

Figure 13: Quenching cross section σ_q of the state $(39, 35)$ with D_2 as a function of the inverse collisional velocity $1/v_{\rm th}$.

molecule at low collisional velocities. The measured quenching cross section with D_2 is proportional – apart from a constant offset $\sigma_{\rm vi}$ – to the inverse velocity $1/v_{\rm th}$, i.e. $\sigma_q - \sigma_{\rm vi} \propto 1/v_{\rm th}$ – see Fig. 13. This is in agreement with the Wigner threshold law of exothermic reactions involving neutral particles. Unfortunately, there are no theoretical calculations on the $\overline{p}{\rm He}^+$–H_2 or $\overline{p}{\rm He}^+$–D_2 system which would investigate the above-mentioned increased attraction at low collisional velocities and therefore it is not known whether it can significantly increase the quenching cross section and whether it really follows the $1/v_{\rm th}$ law.

5 Development of an ultra-slow antiproton beam

ASACUSA is preparing an ultra-slow monoenergetic antiproton beam by sequentially combining the beams from the AD (down to 5.3 MeV), the RFQD (Radio-Frequency Quadrupole Decelerator; down to 50–120 keV), and confining them in a MRT (multi-ring electrode trap) installed in a superconducting magnet of 2.5 T. Here they are cooled and compressed before being extracted, reaccelerated to eV-scale energies and delivered via a beam transport line to gas or solid targets. The MRT, the superconducting solenoid and eV-beam transport line are jointly known as "MUSASHI", or the Monoenergetic Ultra-Slow Antiproton Source for High-precision Investigations. MUSASHI will open a new research field of collision dynamics to be studied in processes like antiprotonic atom formation and ionization processes under 'single collision conditions'.

During 2003, we successfully trapped and stacked millions of antiprotons in the trap. The numbers increased by a factor two compared with the previous year. Antiprotons were then cooled and were extracted from the trap. Approximately 60,000 antiprotons per 'cycle' (= typically 2 AD shots) at 250 eV could be extracted from the strong trap field and detected by an MCP (multi-channel plate) detector in the beam line, placed 1.7 m downstream from the trap center.

Since the 'single collision' experiments require an order of magnitude more antiprotons, most of the beam time was spent to improve the extraction efficiency. We have identified possible sources of the problem, as discussed below. Efforts to improve the extraction efficiency will continue in 2004.

5.1 Beam transport into the trap

Antiprotons need to be confined in a small volume with a radius of 1 mm in the high magnetic field in order for them to be extracted efficiently from the trap field. In order to fulfill that condition, the antiproton beam leaving the AD and entering the trap via the RFQD must be of extremely good quality, i.e., both its emittance and its energy spread must be small. Unfortunately that was not the case in the previous years, and proper beam tuning became possible only this year.

5.1.1 Beam diagnostic devices

We have several devices for diagnosis of the antiproton beams extracted from the AD machine at 5.3 MeV (HEBT) and after the RFQD at 100 keV (LEBT).

i) Scintillation screens (Watchdogs) newly installed with several holes at different diameters are placed at two positions in the 5.3-MeV beamline, and the beam profile is observed using a CCD camera.

ii) Two microwire secondary emission chambers are placed downstream of RFQD, to measure the beam diameter and emittance of the 100-keV decelerated beam non-destructively.

iii) A high-speed Cherenkov counter is used to measure the longitudinal time-structure

of the antiproton beam, downstream of a 200-MHz radiofrequency bunching cavity.

iv) An ultra-thin foil detector is placed in the superconducting, cryogenic environment of the MRT, to measure the beam profile inside the trap.

5.1.2 Improved beam transport into the trap

The beam transport of the 5.3-MeV beam into the RFQD and the 100-keV beam out of the RFQD into the trap has been dramatically improved. This achievement was due to the improved diagnosis of the beams as described above which facilitated our beam tuning. In the previous years we had a great difficulty in aligning the beam and sometimes we had to spend more than half of our beam time in beam tuning at the beginning of each shift, because daily jitter and drift of beam conditions were too large for our sensitive transport system. At the end of the previous year, one of the pulsed solenoids for focusing the 100-keV beam was found to have been misaligned. This had caused an unnecessarily large steering action, too large in fact to be correctable by the downstream steering dipoles. This year, the magnetic elements were properly realigned by the surveyors (the need for this was already stressed in our last year's Status Report), and now the antiproton beam can be properly focused and centered onto the foil-detector with its diameter of 3 mm (FWHM) both horizontally (X) and vertically (Y) at 2.5 T, as shown in Fig. 14. In the previous year, the beam could never be smaller than 1 cm in even one of the X and Y directions, despite the careful and time-consuming efforts spent on tuning the beam.

5.2 Diagnosis of AD beam

As we suggested in last year's Status Report, we doubted the quality of the 5.3-MeV beam from the AD. Now that the beam can be focused well enough in the strong magnetic field, the emittance of the 5.3-MeV beam from the AD seems to be up to the specified value, although the beam has some halo component. We also checked the longitudinal energy spread of the AD beam by changing the buncher phase of the RFQD. The deceleration efficiency of the RFQD had a fairly sharp dependence on the phase (30 degrees FWHM) of the buncher, corresponding to an energy spread of about 5 keV, which should be small enough for our purpose (see Fig. 15). This is in contrast to the previous year when the deceleration efficiency had a very weak dependence on the phase, and hence a much larger energy spread.

5.3 Increased trapping efficiency

The improved beam tuning increased the trap efficiency significantly. In the previous year, as many as 0.6×10^6 antiprotons were lost into annihilation in the first 10–20 s after injection, during the process of cooling down to sub-eV energy. This loss reduced by a factor three in 2003, and the survival rate of antiprotons at the time of extraction increased. Also the number of trapped antiprotons increased, possibly on account of increased deceleration efficiency and improved beam emittance in the RFQD, as well as better focusing at the LEBT. We trapped $(0.7\text{–}1.0) \times 10^6$ antiprotons per AD shot, stably

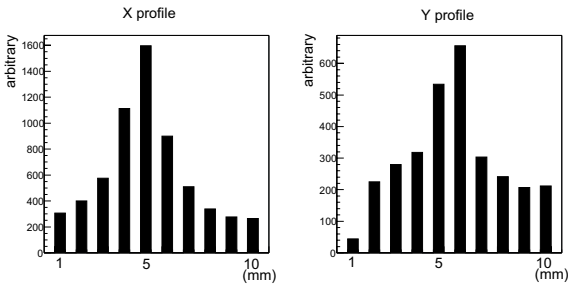

Figure 14: Two-dimensional (X and Y) profiles of the 110 keV antiproton beam after the RFQD observed by the foil-detecter in the magnetic field of 2.5 T. The beam can be centered and well focused.

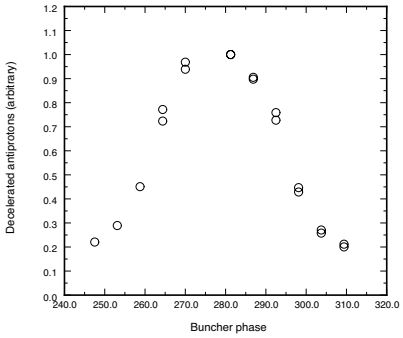

Figure 15: The deceleration efficiency of the RFQD plotted vs. the RFQ buncher phase (in degree). The energy spread of the antiproton beam extracted from the AD was estimated as 5 keV from this measurement.

until the end of our trap cycle of about 1 minute. This number is to be compared with a typical number of 0.3 and maximum 0.6×10^6 the previous year. We then tried stacking of antiprotons and succeeded in stacking up to 5 shots without any losses, achieving a world record by trapping a total of 4.5×10^6 antiprotons.

5.4 Monitoring cooling process of antiprotons

In order to cool the antiprotons from several keV to less than an electronvolt, an electron plasma is loaded in the harmonic trap potential. Measuring the time-dependence of plasma modes excited by the injected antiprotons can then give information on the plasma size and shape as well as the temperature of the electrons, and also constitutes a non-destructive real-time monitor of the cooling process of the antiprotons by electron plasma. We have successfully observed axially symmetric plasma modes (n,0) up to $n = 7$, and the plasma parameters can be calculated from the set of frequencies. Then the shift of frequencies with elapsed time since the antiproton injection manifests the evolution of the plasma temperature. Fig. 16 shows an observed frequency shift of the (2,0) mode which has one node along the axial direction of the spheroidal plasma. As the electron plasma received energy from the incident antiprotons, the frequency first increased, then leveled off for about 10 s before it decreased with a time constant of 15–20 s. The time evolution of the plasma frequencies of the (2,0) and (3,0) modes during cooling after the heat-up was consistently reproduced by calculations [37] which took into account the synchrotron radiation cooling of electrons and the energy transfer between antiprotons and the electron plasma, and a maximum temperature rise of about 0.6 eV was evaluated [38], as shown in Fig. 17. This is the first successful measurement using a trap of two different particles with the same charge, which is expected to provide useful information in the field of non-neutral plasma physics.

The plasma mode (1,0) corresponds to the center-of-mass motion of the plasma in the harmonic potential, and its frequency does not depend on the plasma temperature.

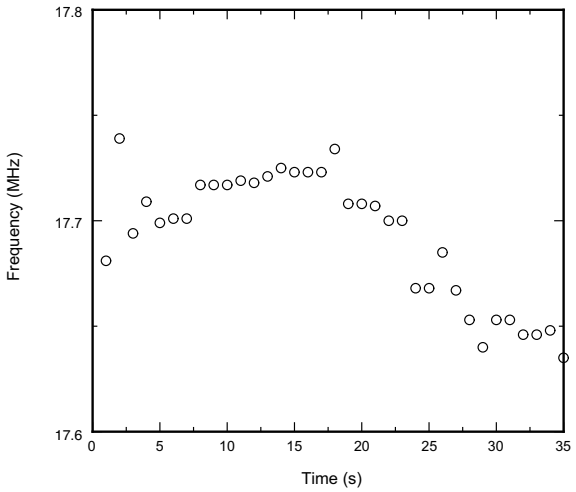

Figure 16: Frequency shift of the (2,0) mode of the electron plasma plotted against elapsed time since antiproton injection.

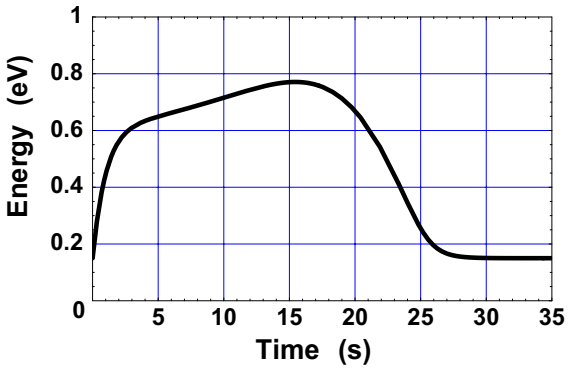

Figure 17: Calculated temperature variation of the electron plasma, showing a maximum temperature rise of about 0.6 eV.

Any change in the frequency should be attributed to the change in the effective potential caused by variations of the charge distribution of the plasma. Fig. 18 shows an example of observed fast Fourier transform (FFT) signals (i.e. power spectra) of the (1,0) mode. Interesting features are that (a) a second peak (S) appeared at a lower frequency next to the main peak (P) at early times, (b) which disappeared later while the main peak shifted slightly (c) until again a secondary peak appeared at about 50 s after antiproton injection. The data are now under analysis, and they are expected to reveal the evolution of the size of the antiproton cloud in the trap. It indicates that the antiproton radial distribution moves outward, resulting in their becoming radially separated from the electron plasma. The distribution consequently broadens, as can be expected for non-neutral plasma fields. If that is the case, we should try to extract the antiproton before the radial separation occurs, because it is known from calculations that only the antiprotons confined in a radius of 1 mm can be extracted out of the strong magnetic field where the field line diverges.

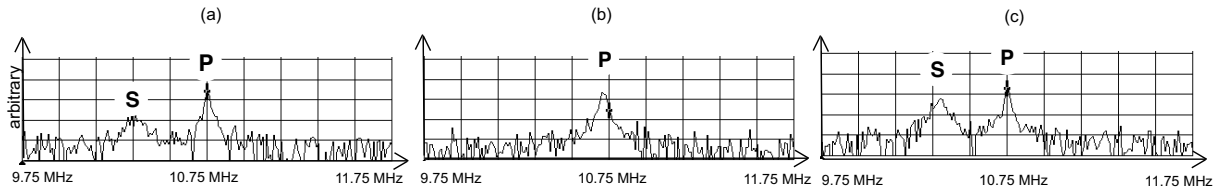

Figure 18: Observed FFT spectra of the (1,0) mode of the electron plasma oscillation at different times after antiproton injection. Observed shift of the main peak (P) in Fig. (b) and appearance of a second peak (S) in Fig. (c) indicate possible radial brow-up and separation of the antiproton cloud away from the electron plasma.

5.5 Extraction of 250 eV antiprotons

Our extraction beamline was designed for transport of ultra-slow antiprotons extracted from the MRT at variable energies between 10 and 1500 eV [39]. We chose the beam energy of 250 eV for optimum transport. The beam was sharply focused 3 times by three Einzel lenses and one asymmetric lens, where variable apertures were installed for differential pumping of 6 orders of magnitude in vacuum pressure.

We have the following detectors for diagnosis of the ultra-slow antiproton beam after the trap.

i) A micro-channel plate (MCP) combined with a delay-line position sensitive detector was placed downstream of the MRT. This detector was sensitive enough to allow counting of single antiprotons, giving two-dimensional images of ultra-slow antiproton beams.

ii) A scintillation counter was placed close to the MCP to detect pions from antiproton annihilation for coincidence purpose, which allowed proper estimation of the number of antiprotons by discriminating possible signals from electrons, negative ions (mainly H^- if any) or decay of radioactive nuclei created by antiproton irradiation.

Only signals from antiproton annihilation can trigger both detectors at the same time, so that a pure image of the antiproton beams can be obtained.

We detected 30,000–45,000 (maximum 60,000) antiprotons per cycle at 250 eV by the MCP detector downstream in 2003, in comparison to 10,000 the previous year. This improvement is due partly to the increased trapping efficiency and partly to the better extraction efficiency resulting from the improved focusing of the incident beam described above.

Although 250-eV antiprotons were successfully extracted from the trap, the extraction efficiency remained quite low (currently 4–6%). The remainder (and major part) of the antiprotons hit the extractor electrodes at the exit of the magnetic field, presumably because they were not confined in a small enough diameter in the trap at the strong magnetic field. We have so far tried several techniques to compress the antiproton cloud before extraction, such as plasma rotation and side-band cooling. We also tested different potential ramping schemes and different magnetic field strengths, but these did not further improve the extraction efficiency. One of possible reasons for the failure to compress the plasma is that the plasma was heated to too high a temperature, and the density distribution became too large. We also note that in order for the compression to work effectively, the excess heat must be taken away from the plasma, and in usual cases some residual gases play an important role as a coolant. For the case of antiprotons, however, this technique of buffer-gas cooling cannot be applied because they are subject to annihilation against gas atom/molecule. Certainly another mechanism for heat dissipation of the plasma, which should work under our ultra-high vacuum of better than 10^{-12} Torr, must be developed.

As stated above, the frequency shift observed in plasma oscillations of the electrons revealed possible radial separation of the electron and antiproton plasmas and broadening of the antiproton cloud, at a time typically about 40 s after injection. A possible cause

of the problem in the current system could be that the preloaded electron plasma has a rather large diameter of 1 cm. It may then happen that the antiproton cloud broadens during the cooling process of thermal mixing with the electrons. The best way of avoiding this would be to prepare an electron plasma with a smaller diameter, and we are planning to make this modification to our electron injection system for 2004.

6 Stopping Power Measurements.

The slowing down of ions in matter is generally caused by collisions with the target electrons, leading to ionization or excitation. For slow projectiles passing through metals, the target conduction electrons can be considered as a free electron gas, and the energy loss per path length (the so-called stopping power) will be proportional to the velocity of the projectile due to the "frictional" nature of the interaction. The confirmation of this result has been hampered until now by the fact that slow positive ions (such as protons) do not have a well defined charge while passing through matter due to electron capture and loss processes. In order to firmly establish the foundation of stopping power theory, we therefore measured the stopping power of slow antiprotons in a number of thin, metallic targets: C, Al, Ni, and Au [40] and later refined the technique to obtain more accurate data. For the targets mentioned, the stopping power proved to be velocity proportional down to antiproton energies around 2 keV. For insulators, on the other hand, the target electrons have a minimum excitation energy (band gap or excitation potential) and therefore, it was expected that the free electron gas model should fail there. This was actually observed for protons passing through gaseous targets of He and Ne [41,42], manifested as a "knee" in the stopping power curve, with a much steeper than velocity proportional dependence below the knee. However, surprisingly no such effect was observed for the insulators LiF, Al_2O_3 and SiO_2 [43]. This was suggested to be due to a formation, during the passage of the target, of "pseudo molecules" consisting of a target atom and the projectile proton – leading to a lowering of the energy difference between the highest occupied and the lowest unoccupied electronic state in the target. In order to test this idea, we measured [44] the stopping power of LiF for antiprotons, and found that it is very closely proportional to the projectile velocity, as seen in figure 19. The slopes of the fitted curves in figure 19 are

Protons on LiF	0.96 ± 0.04 (eV/Å)
Antiprotons on LiF	1.10 ± 0.10 (eV/Å)
Antiprotons on Al	0.97 ± 0.03 (eV/Å)

As can be seen, there is no departure from a value of one for the antiproton on LiF case. This casts serious doubt on the validity of the above-mentioned model, because antiprotons do not form pseudo molecules with atoms due to their negative charge. Hence better models of the slowing down of slow ions in insulators are gravely needed. An outstanding question which was left after our measurements on LiF targets was the validity of the absolute values of our measured stopping powers. Since the stopping power is deduced as the energy loss divided by the target thickness, and since we are very sure of the correctness of the energy loss measurement, there might be uncertainties in our

measurement of the absolute thickness of our targets (typically 200 – 400 Å thick). This question came up when we compared our proton data with the proton data by the Linz group [43], which were almost a factor of two larger [44]. After having performed several tests and measurements of our target thicknesses (see figure 20), we conclude that our measurements are correct.

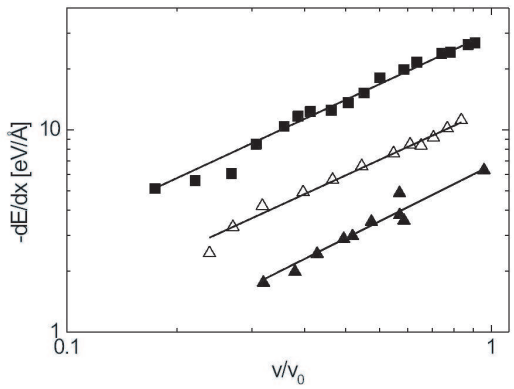

Figure 19: Our measured stopping powers for antiprotons on LiF (filled triangles) , for protons on LiF (open triangles) and for antiprotons on Al (squares). The Al data have been multiplied by 4 for clarity.

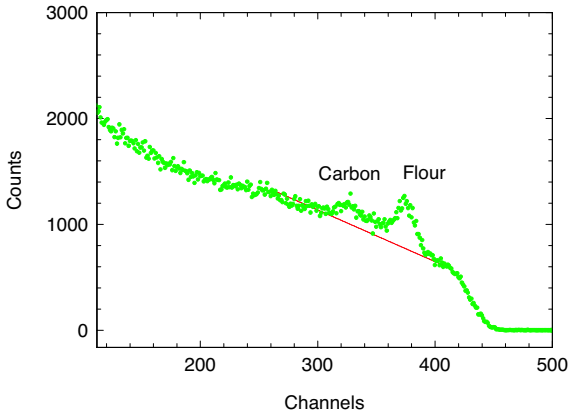

Figure 20: Spectrum of 350 keV protons 160° backscattered from one of our LiF targets. From the "Flour" peak we calculate the thickness to be (375 ± 20) Å for this foil with a nominal thickness of 400 Å.

Part II
Plans for 2004

1 PPB-scale laser spectroscopy of $\overline{p}\mathrm{He}^+$ atoms

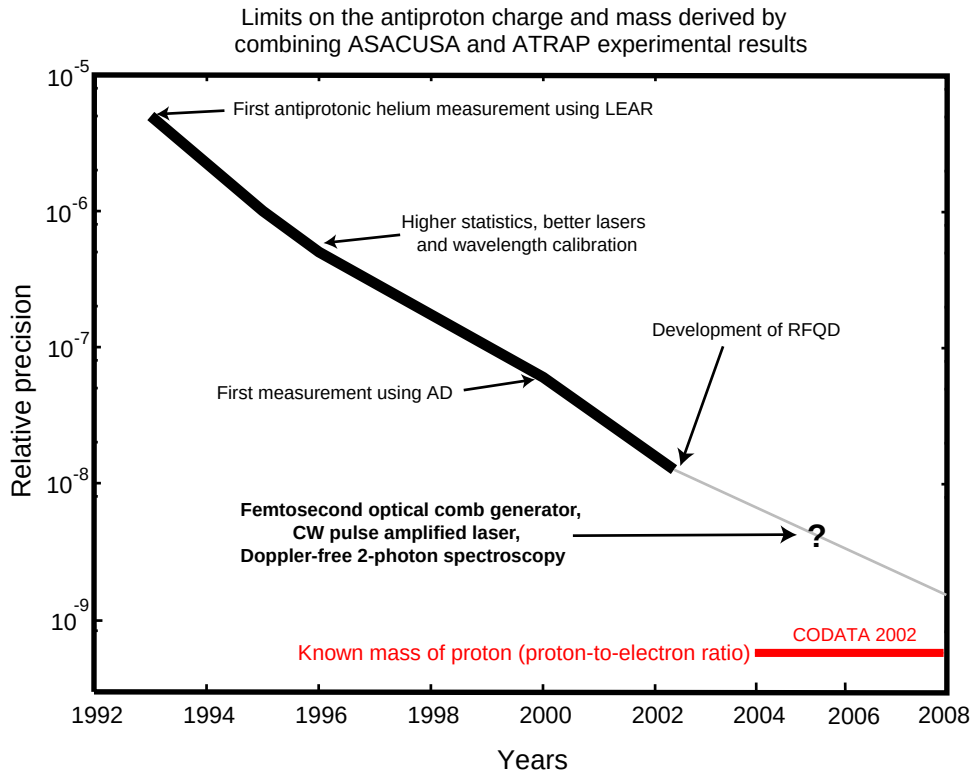

Figure 21: Relative precision on the possible differences between the antiproton mass and charge measured over the years. The results were derived by combining the results of laser spectroscopy experiments on $\overline{p}\mathrm{He}^+$ atoms, with those of Penning trap experiments by the TRAP collaboration.

In 2004, we plan to measure the transition frequencies of $\overline{p}\mathrm{He}^+$ to higher precision than before, using a new femtosecond optical-frequency comb generator [45, 46] and a constant-wave pulse-amplified titanium sapphire laser. In Fig. 21, limits $\delta_{\overline{p}}$ on the possible differences between the antiproton mass $M_{\overline{p}}$ and charge $Q_{\overline{p}}$ and those of the proton's (M_p and Q_p) derived from measurements of $\overline{p}\mathrm{He}^+$ over the years

$$\delta_{\overline{p}} = \frac{Q_p + Q_{\overline{p}}}{Q_p} \sim \frac{M_p - M_{\overline{p}}}{M_p} \tag{6}$$

are shown; the current limit is 10 ppb. The physical constants tabulated in the CODATA database (the values revised this year) give the alpha particle-proton mass ratio

$$m_\alpha/m_p = 3.97259968907(52) \tag{7}$$

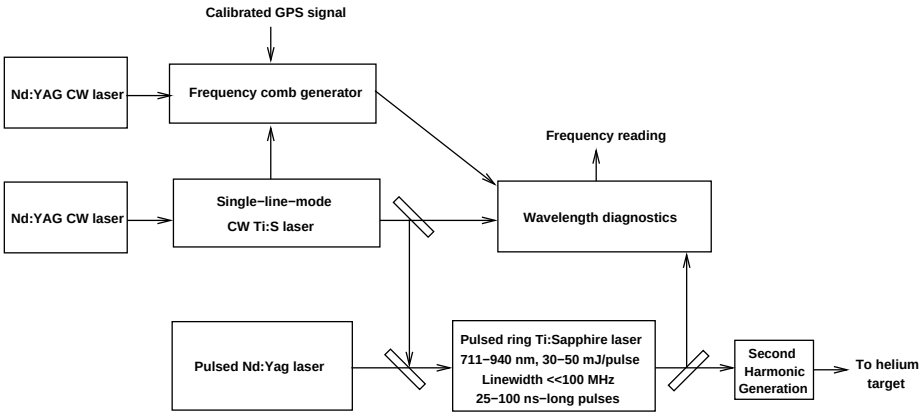

Figure 22: Schematic layout of the high-precision laser system currently developed at CERN.

measured to a relative precision of 0.13 ppb, and on the electron-proton mass ratio

$$m_e/m_p = 5.4461702173(25) \times 10^{-4} \tag{8}$$

with a precision of 0.46 ppb.

The central values are used to determine starting values of the laser frequency scans for resonantly induced transitions in $\overline{p}\mathrm{He}^+$, but their own errors do not influence our determinations of the antiproton charge and mass. Therefore, if the precision of our $\overline{p}\mathrm{He}^+$ experiments were improved by a factor of ~ 20 and a $\delta_{\overline{p}} < 0.5$ ppb limit reached, the antiproton mass (or more exactly the electron-to-antiproton mass ratio $m_e/m_{\overline{p}}$) would be more precisely known than the corresponding value of the proton given in Eq. 8.

To achieve these higher precisions, we are developing a new laser system (Fig. 22) with an energy resolution 100 times higher than those used previously [47]. It consists of i): a constant-wave, single-line mode titanium sapphire or dye laser with a frequency bandwidth $\delta f/f < 10^{-10}$, ii): a femtosecond optical comb generator system which measures the frequency of the above laser with a relative accuracy of $\sim 10^{-12}$, iii): a pulse amplifier which converts the CW laser light into high-energy pulses with peak powers of 0.1–1 gigawatt. The first measurements of $\overline{p}\mathrm{He}^+$ using the laser will be carried out in 2004.

2 Further studies of $\overline{p}\mathrm{He}^{2+}$ ions, and attempts at laser spectroscopy

In 2004 we plan to continue systematic studies of the $\overline{p}\mathrm{He}^{2+}$ ion described in the first pages of this report, and will attempt the first laser spectroscopy of this unique and promising Bohr-type ion. We are currently carrying out computer simulations and technical studies to evaluate the feasibility of these experiments, but a likely method involves i): producing large numbers of cold $\overline{p}\mathrm{He}^{2+}$ using the laser-induced ionization method demonstrated in 2003, as described above ii): irradiating the ion with a separate laser pulse, thus inducing transitions between $\overline{p}\mathrm{He}^{2+}$ states. The experiment is difficult

since the $\bar{p}He^{2+}$ wavelengths lie in the vacuum ultraviolet (VUV) region $\lambda < 200$ nm which are rapidly absorbed in air. Frequency mixing in various types of non-linear laser crystals or noble gases will be used to produce the VUV light, and an evacuated beamline may be necessary to transport the laser beam to the experimental target.

3 Plans for the Trap in 2004

As is described in the status report, the trap group is working hard to improve the extraction efficiency of the trapped/cooled antiprotons. It is noted that the total number of stably trapped antiprotons per one AD shot has been growing consistently every year. At the same time, an effective number of available antiprotons per unit time improved several times by applying a stacking technique. Actually, the maximum number of accumulated antiprotons reached something like 5 million, the world largest ever achieved. In 2004, we will extract slow antiprotons with much higher efficiency by installing

(1) a movable on-axis electron gun

(2) a high-Q tank circuit at the antiproton trap

(3) a movable screen downstream of the trap to monitor the antiproton and electron plasma shapes

(4) a special purifying filter of liquid helium to prevent blocking of the needle valve

(1) Installation of a movable on-axis electron gun: The electron accumulation scheme has been studied consistently by off-line measurements in Japan. It was found that the accumulation rate and accordingly the accumulation number increase exponentially as is shown in Fig. 3 when an electron gun is located near the axis of the superconducting solenoid. With this scheme, the time to accumulate more than 10^{10} electrons is just a fraction of a second. Furthermore, the radial size of the electron plasma so formed is $\sim$ 1mm, which is expected to reduce the size of the cooled antiproton cloud, and accordingly to improve the extraction efficiency of antiprotons drastically.

(2) Installation of a high-Q tank circuit: Although the accumulation technique has more or less been established, efficient extraction evidently needs further development. Once a large number of cold antiprotons are stably accumulated, electrons used to cool antiprotons should be kicked out (1) to avoid the radial expansion of the antiproton cloud and (2) to suppress the diocotron instability during slow extraction, which kills a considerable fraction of antiprotons in the trap due to $E \times B$ drift and at the same time prevents stable extraction. After the electron kick out, antiprotons will be compressed by a side-band cooling technique, which however heats up the antiproton cloud and eventually prevents compression of the cloud. Usually some residual gas is used as a coolant to remove the heat during compression, which however does not work in the present case, where all the procedures are done under extremely high vacuum. In order to remove heat under extreme high vacuum, a high-Q tank circuit is in preparation and will be added to the harmonic part of the trap, which will allow efficient resistive cooling. This technique has been tested with protons in a similar trap, and will be applied to the MUSASHI trap.

(3) Installation of a movable screen downstream of the trap: A movable phosphor screen is prepared and will be inserted from the downstream transport beam line into the trap to monitor the size, shape, and their time evolutions of the electron plasma and the antiproton cloud.

(4) Installation of a special purifying filter for liquid helium (LHe) in its transport tube: It appears that the quality of LHe got worse, and the needle valve for the bore temperature control consequently became blocked several times in 2003, resulting in a very short antiproton lifetime, and preventing us from studying various important phenomena which need observation times longer than several minutes. These include the side-band compression of the antiproton cloud, multiple stacking, slow extraction, etc. We are now developing a special purifying filter to be attached to the LHe transport tube so that the experiment can be done under stable conditions (collaboration with the Komaba Low Temperature Laboratory of University of Tokyo.)

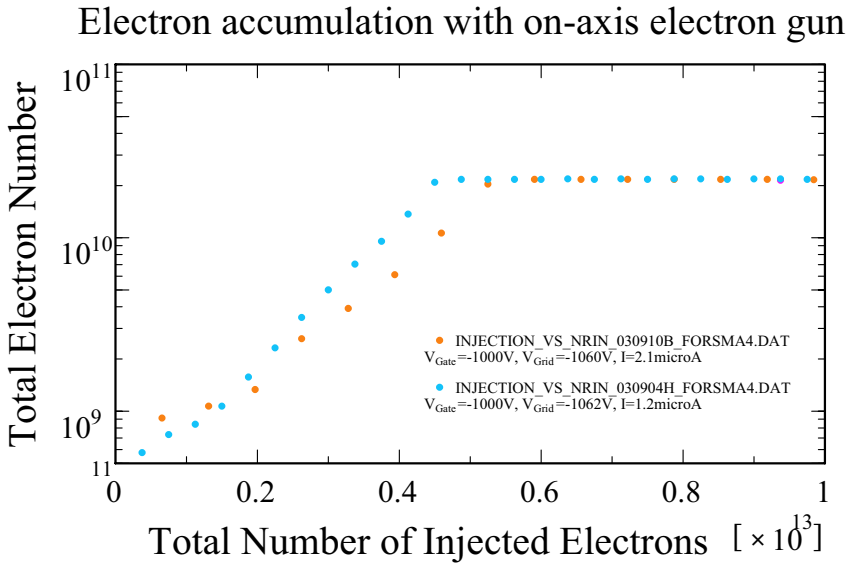

Figure 23: Total number of electrons accumulated as a function of injection electron number.

4 Ionization cross section measurements

As described in our earlier status reports, there is a great need to create benchmark data for the fundamental theoretical description of ionization processes involving the simplest possible collision systems: Antiprotons on atomic hydrogen and helium. This is especially true for the case where the projectile is slow, in the sense that it moves with a velocity smaller than that of the active electron. Figure 24 shows, that there is a great deal of uncertainty in the theoretical calculation of even the total cross section for ionization, in this case for antiprotons colliding with helium. A similar situation exists for the ionization of atomic hydrogen. In order to create such benchmark data, we have built an apparatus in which an antiproton beam crosses a jet of the target atoms. The

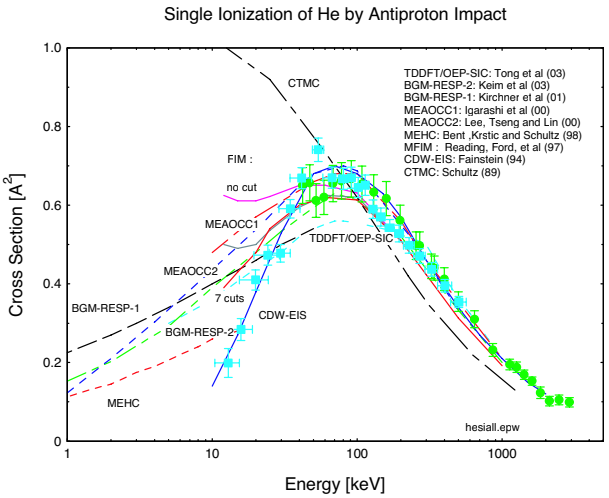

Figure 24: Our measured cross sections for the single ionization of helium by antiproton impact (filled squares and circles) compared with a number of advanced calculations.

ions created by ionization are extracted from the interaction region and their Time-of-Flight is recorded. The original plan (see ASACUSA status report 2002) was to extract eV antiprotons as a DC beam from the MUSASHI Penning trap, and to accelerate them onto our target by applying a positive high voltage to our system. Since the technique of extraction from the trap has not yet reached its design values, we have during 2003 designed an electrostatic analyzer, which will be placed between the RFQD+LEBT and our apparatus, such that we can obtain pulses of antiprotons of 200 nsec width, and a 10% energy spread. This removes the need to raise the platform to high voltage. It also broadens our TOF measurement (which is now started with the AD trigger pulse) by 200 nsec, but this is not expected to have any serious impact on the results. The measurement of the cross section includes the determination of the terms in the equation

$$N = N_{\overline{p}} \sigma n l \epsilon$$

Where N is the number of ions of the proper mass-to-charge ratio, $N_{\overline{p}}$ is the number of antiprotons passing through the target, σ the cross section, nl the product of target density and length and ϵ the effectiveness of the ion detector. Using a pulsed electron beam and known cross sections for ionization by keV electron impact, we can determine $nl\epsilon$. Since we cannot count the $\sim 10^6$ antiprotons in an energy-selected pulse from the AD, we have to use an integrated signal from our projectile MCP detector as normalization. This signal will be calibrated using impact of 30-40 keV antiprotons, because for such projectiles the cross section is known (see figure 24). In order to avoid that two (or more) ions are created in a single shot, we have asked the AD staff to prepare an extraction mode such that each extraction will consist of 9 "subextractions" which each will deliver to our apparatus 10^5 antiprotons. With typical numbers for helium: $n = 10^{12}$ cm^{-3}, $l = 1$cm, $\epsilon = 1$ and $\sigma = 2 \times 10^{-17}$cm^2 we then expect to reach easily 1 count per AD extraction. For a datum with 10% accuracy we therefore need 100 AD shots, or 3 hours of beam time. Figure 25 shows the newly designed 60° electrostatic analyzer, which has a 10% energy

resolution, and is matched to the optics of the RFQD+LEBT and via an Einzel lens to our apparatus.

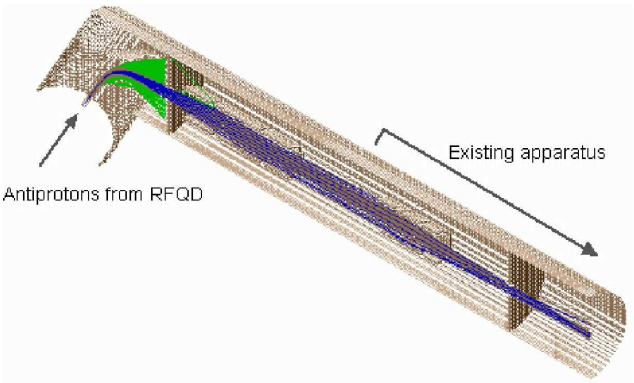

Figure 25: A SIMION simulation of the energy selection and transport of antiprotons from the RFQD+LEBT to our apparatus.

References

[1] M. Iwasaki, S. N. Nakamura, K. Shigaki, Y. Shimizu, H. Tamura, T. Ishikawa, R. S. Hayano, E. Takada, E. Widmann, H. Outa, M. Aoki, P. Kitching, and T. Yamazaki, Phys. Rev. Lett. 67 (1991) 1246.

[2] N. Morita, K. Ohtsuki, and T. Yamazaki, Nucl. Instrum. Methods Phys. Res., Sect. A 330 (1993) 439.

[3] T. Yamazaki, N. Morita, R. S. Hayano, E. Widmann, and J. Eades, Phys. Rep. 366 (2002) 183.

[4] M. Hori, J. Eades, E. Widmann, H. Yamaguchi, J. Sakaguchi, T. Ishikawa, R. S. Hayano, H. A. Torii, B. Juhász, D. Horváth, and T. Yamazaki, Phys. Rev. Lett. 87 (2001) 093401.

[5] M. Hori, J. Eades, R. S. Hayano, T. Ishikawa, W. Pirkl, E. Widmann, H. Yamaguchi, H. A. Torii, B. Juhász, D. Horváth, and T. Yamazaki, Phys. Rev. Lett. 91 (2003) 123401.

[6] V. I. Korobov, Phys. Rev. A 54 (1996) R1749.

[7] Y. Kino, N. Yamanaka, M. Kamimura, and H. Kudo, Hyperfine Intractions 138 (2001) 179.

[8] V. Korobov, Phys. Rev. A 67 (2003) 062501.

[9] G. Gabrielse, A. Khabbaz, D. S. Hall, C. Heimann, H. Kalinowsky, and W. Jhe, Phys. Rev. Lett. 82 (1999) 3198.

[10] R. Landua and E. Klempt, Phys. Rev. Lett. 48 (1982) 1722.

[11] T. B. Day, G. A. Snow, and J. Sucher, Phys. Rev. Lett. 3 (1959) 61.

[12] G. Reifenröther, E. Klempt, and R. Landua, Phys. Lett. B 203 (1988) 9.

[13] T. Jensen and V. Markushin, private communication, 2002.

[14] H. Yamaguchi *et al.*, Phys. Rev. A 66 (2002) 022504.

[15] E. Widmann, J. Eades, T. Ishikawa, J. Sakaguchi, T. Tasaki, H. Yamaguchi, R. Hayano, M. Hori, H. Torii, B. Juhász, D. Horváth, and T. Yamazaki, Phys. Rev. Lett. 89 (2002) 243402.

[16] D. Bakalov and V. I. Korobov, Phys. Rev. A 57 (1998) 1662.

[17] V. Korobov and D. Bakalov, J. Phys. B: At. Mol. Opt. Phys. 34 (2001) L519.

[18] Y. Kino, N. Yamanaka, M. Kamimura, and H. Kudo, in *Proceedings of the 3rd European Conference on Atomic Physics at Accelerators (APAC2001)*, Aarhus, Denmark, 2001, Hyperfine Interactions, in press.

[19] A. Kreissl, A. D. Hancock, H. Koch, T. Köhler, H. Poth, U. Raich, D. Rohmann, A. Wolf, L. Tauscher, A. Nilsson, M. Suffert, M. Chardalas, S. Dedoussis, H. Daniel, T. von Egidy, F. J. Hartmann, W. Kanert, H. Plendl, G. Schmidt, and J. J. Reidy, Z. Phys. C 37 (1988) 557.

[20] H. A. Torii, R. S. Hayano, M. Hori, T. Ishikawa, N. Morita, M. Kumakura, I. Sugai, T. Yamazaki, B. Ketzer, F. J. Hartmann, T. von Egidy, R. Pohl, C. Maierl, D. Horváth, J. Eades, and E. Widmann, Phys. Rev. A 59 (1999) 223.

[21] G. Ya. Korenman, Elastic scattering and collisional shift of hfs transitions of metastable antiprotonic helium, in *Abstract Book of the Asia-Pacific Few Body Conference (APFB99), Kashiwa, 1999*, page 112.

[22] G. Ya. Korenman, N. Yudin, and S. Yudin, NIM B (2004), proceedings of LEAP03.

[23] D. D. Bakalov, private communication, 2001.

[24] J. Sakaguchi, PhD thesis, University of Tokyo, 2003.

[25] B. Juhász, J. Eades, R. Hayano, M. Hori, D. Horváth, T. Ishikawa, H. Torii, E. Widmann, H. Yamaguchi, and T. Yamazaki, Chem. Phys. Lett. 379 (2003) 91.

[26] B. Juhász, J. Eades, R. Hayano, M. Hori, D. Horváth, T. Ishikawa, H. Torii, E. Widmann, H. Yamaguchi, and T. Yamazaki, Nucl. Instrum. Methods B 214 (2004) 91. .

[27] S. Sauge and P. Valiron, Chem. Phys. 283 (2002) 433.

[28] R. S. Hayano, F. E. Maas, H. A. Torii, N. Morita, M. Kumakura, T. Yamazaki, H. Masuda, I. Sugai, F. J. Hartmann, H. Daniel, T. von Egidy, B. Ketzer, W. Müller, W. Schmid, D. Horváth, J. Eades, and E. Widmann, Phys. Rev. Lett. 73 (1994) 1485, Errata 73 (1994) 3181.

[29] B. Ketzer, F. J. Hartmann, T. von Egidy, C. Maierl, R. Pohl, J. Eades, E. Widmann, T. Yamazaki, M. Kumakura, N. Morita, R. S. Hayano, M. Hori, T. Ishikawa, H. A. Torii, I. Sugai, and D. Horváth, J. Chem. Phys. 109 (1998) 424.

[30] B. Ketzer, T. von Egidy, F. J. Hartmann, C. Maierl, R. Pohl, J. Eades, E. Widmann, T. Yamazaki, M. Kumakura, N. Morita, R. S. Hayano, M. Hori, T. Ishikawa, H. A. Torii, I. Sugai, and D. Horváth, Europ. Phys. J. D 13 (2001) 305.

[31] R. Pohl, F. J. Hartmann, B. Ketzer, T. von Egidy, C. Maierl, J. Eades, E. Widmann, T. Yamazaki, M. Kumakura, N. Morita, R. S. Hayano, M. Hori, T. Ishikawa, H. A. Torii, I. Sugai, and D. Horváth, Phys. Rev. A 58 (1998) 4406.

[32] J. E. Russell, Phys. Rev. A 1 (1970) 742.

[33] T. Yamazaki and K. Ohtsuki, Phys. Rev. A 45 (1992) 7782.

[34] V. I. Korobov and I. Shimamura, Phys. Rev. A 56 (1997) 4587.

[35] O. Kartavtsev, D. Monakhov, and S. Fedotov, Phys. Rev. A 61 (2000) 062507, Errata 61 (2000) 019901(E).

[36] Y. Kino, M. Kamimura, and H. Kudo, Nucl. Instrum. Methods Phys. Res., Sect. B, in press. .

[37] H. Higaki, N. Kuroda, T. Ichioka, K. Y. Franzen, Z. Wang, K. Komaki, and Y. Yamazaki, Phys. Rev. E 65 (2002) 04610.

[38] N. Kuroda, H. A. Torii, K. Y. Franzen, Z. Wang, S. Yoneda, M. Inoue, M. Hori, B. Juhász, D. Horváth, H. Higaki, A. Mohri, J. Eades, K. Komaki, and Y. Yamazaki, submitted to Phys. Rev. Lett. .

[39] K. Y. Franzen, N. Kuroda, H. A. Torii, M. Hori, Z. Wang, H. Higaki, S. Yoneda, B. Juhász, D. Horváth, A. Mohri, K. Komaki, and Y. Yamazaki, Rev. Sci. Instrum. 74 (2003) 3305.

[40] S. Møller, A. Csete, T. Ichioka, H. Knudsen, U. Uggerhøj, and H. Andersen, Phys. Rev. Lett. 88 (2002) 193201.

[41] R. Golser and D. Semrad, Phys. Rev. Lett. 66 (1991) 1831.

[42] A. Schiefermüller *et al.*, Phys. Rev. A 48 (1993) 4467.

[43] K. Eder *et al.*, Phys. Rev. Lett. 79 (1997) 4112.

[44] S. Møller, A. Csete, T. Ichioka, H. Knudsen, U. Uggerhøj, and H. Andersen, Submitted to Phys Rev Letters (Nov.2003) .

[45] R. Holzwarth, T. Udem, T. Hänsch, J. Knight, W. Wadsworth, and P. Russel, Phys. Rev. Lett. 85 (2000) 2264.

[46] T. Udem, R. Holzwarth, and T. Hänsch, Nature 416 (2002) 233.

[47] M. Hori *et al.*, Optics Letters 28 (2003) 2479.